

See discussions, stats, and author profiles for this publication at: <https://www.researchgate.net/publication/255750788>

# Shock-wave induced damage in lipid bilayers: a dissipative particle dynamics simulation study. Soft Matter

ARTICLE *in* SOFT MATTER · APRIL 2011

Impact Factor: 4.03 · DOI: 10.1039/C0SM01296C

---

CITATIONS

15

---

READS

48

## 3 AUTHORS:



[Georg Ganzenmueller](#)

Fraunhofer Institute for High-Speed Dynam...

20 PUBLICATIONS 236 CITATIONS

SEE PROFILE



[Stefan Hiermaier](#)

Fraunhofer Institute for High-Speed Dynam...

64 PUBLICATIONS 317 CITATIONS

SEE PROFILE



[Martin Oliver Steinhauser](#)

Fraunhofer Institute for High-Speed Dynam...

32 PUBLICATIONS 329 CITATIONS

SEE PROFILE

Cite this: *Soft Matter*, 2011, **7**, 4307[www.rsc.org/softmatter](http://www.rsc.org/softmatter)

PAPER

# Shock-wave induced damage in lipid bilayers: a dissipative particle dynamics simulation study

G. C. Ganzenmüller,\* S. Hiermaier and M. O. Steinhauser

Received 10th November 2010, Accepted 18th February 2011

DOI: 10.1039/c0sm01296c

The effects of shock-wave impact on the damage of lipid bilayer membranes are investigated with dissipative particle simulations at constant energy (DPDE). A coarse-grained model for the phospholipid bilayer in aqueous environment is employed, which models single lipids as short chains consisting of a hydrophilic head and two hydrophobic tail beads. Water is modeled by mapping four H<sub>2</sub>O molecules to one water bead. Using the DPDE method enables us to faithfully simulate the non-equilibrium shock-wave process with a coarse-grained model as the correct heat capacity can be recovered. At equilibrium, we obtain self-stabilizing bilayer structures that exhibit bending stiffness and compression modulus comparable to experimental measurements under physiological conditions. We study in detail the damage behavior of the coarse-grained lipid bilayer upon high-speed shock-wave impact as a function of shock impact velocity and bilayer stability. A single damage parameter based on an orientation dependent correlation function is introduced. We observe that mechanical bilayer stability has only small influence on the resulting damage after shock-wave impact, and inertial effects play almost no role. At shock-front velocities below  $\lesssim 3000 \text{ ms}^{-1}$ , we observe reversible damage, whereas for speeds  $\geq 3900 \text{ ms}^{-1}$  no such recovery, or self-repair of the bilayer, could be observed.

## 1 Introduction

It is well known that exposure of biological cells to shock-waves causes damage to the cell membrane, which may or may not be reversible.<sup>1–5</sup> However, the precise mechanism how this damage arises is not fully understood. There exist two main areas of application relying on shock-wave treatment of cells: in gene therapy, permeabilization of the plasma membrane aims at delivering genes, therapeutic molecules, or genetic material into the cytoplasm.<sup>6</sup> The treatment of cancerous tissue with high intensity focused ultrasound (HIFU) relies on destruction of cells through conversion of mechanical energy into heat (coagulative necrosis), and through mechanical damage induced by acoustic cavitation (formation and implosion of microscopic gas bubbles at the focal point). Cavitation induces shock-waves which can lead to rupture of the cell membrane.<sup>7,8</sup> These applications are of significant importance in cell biology, biochemistry, and medicine. Therefore, it is crucial to understand the precise microscopic mechanisms of how cell membrane damage arises due to shock waves.

Experimentally, it is very difficult to observe the dynamics of membrane rupture: A typical cell membrane has thickness  $d \approx$

5 nm, while the pressure front of a shock wave travels at supersonic speeds, *i.e.* with a velocity  $v_s \gg 1430 \text{ ms}^{-1}$  in water. The time-scale during which a shock wave interacts with a cell membrane is thus on the order of a few picoseconds. These very small time- and length-scales render direct visualization by optical means very difficult. As a consequence, it may prove particularly helpful to elucidate the microscopic structural details and dynamics with computer simulations. However, this as well is a challenging task due to the structural complexity of cell membranes: These are constituted mainly from phospholipids, which form a two-dimensional bilayer, with the hydrophilic phosphate “heads” pointing outwards and interfacing with the aqueous environment, while the hydrophobic “tails” point inwards in order to minimize their exposure to the surrounding water. This structure is essentially a thin fluid layer with immersed proteins and carbohydrates, stabilized by a subtle balance of competing hydrophobic and hydrophilic interactions. Studying the interaction of a shock-wave with a *soft* matter system such as a lipid bilayer is interesting in its own right: as the lipid bilayer is not a rigid body, the shock-wave does not experience a major change in impedance as it traverses the interface between water and bilayer, and it is *a priori* unclear by which mechanisms damage is caused, and how it depends on physical parameters such as shock-wave velocity, shock pulse duration, or shock pulse shape. The purpose of this paper is not to simulate cell membranes in realistic detail, but to focus on a simple model of the major constituent of a cell membrane, which is the

Research Group Shock Wave Effects in Soft Biological Matter, Department of Composite Structures, Fraunhofer Institute for High-Speed Dynamics, Ernst-Mach Institut, EMI, Eckerstraße 4, 79104 Freiburg, Germany. E-mail: georg.ganzenmueller@emi.fraunhofer.de; Fax: +49 761 2714-1440; Tel: +49 761 2714-440

phospholipid bilayer, and to study the response of such a generic model to shock-waves. The standard technique to numerically simulate phospholipid bilayers is molecular dynamics (MD).<sup>9–11</sup> However, in spite of considerable improvement of the method itself and the ever-increasing CPU power over the last decades, it is still only possible to simulate—with atomistic detail—tiny membrane patches, typically involving only a few hundred lipid molecules for time spans of a few nanoseconds.

The existing published research on the largest MD simulations of shock wave interaction with cell membranes<sup>12,13</sup> uses system sizes of 128 phospholipids, with simulation box lengths parallel, and perpendicular to the bilayer plane of  $L_{\parallel} \approx 6.5$  nm and  $L_{\perp} \approx 16.0$  nm, *i.e.*, comparable to the bilayer thickness. It is questionable whether such small systems can quantitatively reproduce real damage processes for several reasons: (i) the employed periodic boundary conditions impose an artificial stabilization of the membrane patch due to correlation effects. (ii) Membrane rupture will likely originate from a defect, *i.e.* a deviation from the ideal flat surface. However, undulations of the membrane are strongly suppressed due to the small simulation box. (iii) As we will show in Sec. 3, the time evolution of the shocked membrane needs to be studied for as long as possible, requiring a large box length  $L_{\perp}$  along the direction of the shock impulse in order to allow the shock front to travel for a long period of time, such that either a slow diffusive disintegration of the membrane, or structural recovery from the induced damage can be observed.

These requirements can best be met by coarse graining the complex molecules into simpler structures, retaining only the physically important features required to study the phenomena of interest.<sup>14,15</sup> This is achieved by replacing entire groups of atoms with single interaction sites, thus lowering the computational work load. Coarse-grained (CG) models have been used with great success for equilibrium properties of membranes,<sup>16</sup> however, the treatment of dynamical properties is much more challenging as we explain in the following. A shock wave can be described as a small region of high pressure, density, and temperature, propagating at supersonic speed through a medium. The pressure gradient at the shock wave front is infinitely steep on a macroscopic length scale, thus giving rise to a first order transition from the low to high pressure regions. A first order transition is always dissipative; therefore, a coarse-grained model for shock-wave studies must also faithfully reproduce the conversion of ordered kinetic energy (the shock-wave impulse) into a corresponding temperature increase, as the shock-wave passes through the medium and is dissipated. It is precisely here, where the difficulty with using MD-based CG models for studying dynamical properties becomes apparent: As the number of degrees of freedom  $N_F$  is reduced by lowering the total number of particles, the heat capacity at constant volume,  $C_V = N_F k_B$  is reduced (assuming quadratic degrees of freedom). This leads to a higher temperature increase due to dissipation in the coarse grained model than is the case when using a full atomistic description. However, reproducing the correct temperature relaxation profiles behind the shock front is of paramount importance if the coarse grained model is to have quantitative predictive character.

In order to resolve this issue, we follow Stoltz<sup>17</sup> by employing a variant of the mesoscopic simulation technique Dissipative Particle Dynamics (DPD).<sup>18,19</sup> DPD is a momentum conserving,

Galilean invariant method which mimics on average the complex particle dynamics of a fully detailed system by incorporating stochastic fluctuations in the equations of motion of the corresponding CG model. However, DPD in its original form is an isothermal method, implying that it cannot be used for adiabatic processes with extremely high temperature gradients which occur during shock wave propagation. This problem was addressed with the DPDE method (Dissipative Particle Dynamics at constant Energy).<sup>20,21</sup> Here, particles carry an internal energy reservoir, which, along with an equation of state relating energy and entropy, defines a heat capacity and temperature for each particle individually. The evolution of the internal energy is constructed such that the total energy, *i.e.*, the sum of potential, internal, and kinetic energies remains constant. The rate of conversion between the particles' internal and kinetic energy governs the dissipation dynamics of the system and can be adjusted to accurately reproduce the shock wave relaxation profile of fully atomistic simulations. This in turn enables us to simulate shock wave induced phenomena on much larger length and time scales than currently possible with atomistic simulations.

This paper is organized as follows. In the next section, we first provide the details of our coarse grained model, then describe our implementation of the DPDE method, and finally explain how shock waves are generated in our simulations. Then, in Section 3, we discuss our simulation results for lipid bilayers of varying stability and conclude this work with an outlook on future improvements and accompanying experiments.

## 2 Methods

### 2.1 Lipid membrane and water system

Lipid bilayer membranes in biological cells are complex structures composed mainly of phospholipids, and, to a lesser extent, of membrane proteins and various carbohydrates. Here, we do not attempt to model all these intricate details. Instead, we employ a simple CG model of a complex phospholipid, which forms stable bilayers that reproduce key mechanical parameters of cell membranes, such as bending rigidity  $\kappa$ , area compression modulus  $K_a$ , rupture strength  $\delta_r$ , and mass density profile. Our model builds on the work of Cooke *et al.*,<sup>22</sup> who presented a simple model of a phospholipid given by three interaction sites: one head and two tail beads (see Fig. 1). This model has the advantage that it can be easily adjusted to yield different membrane rupture strengths and bending rigidities, thus allowing a systematic study of how shock wave induced damage is affected by these mechanical parameters. For convenience we quote the interaction potentials from Ref. 22 here. All beads interact *via* a repulsive Weeks–Chandler–Andersen potential, which provides mechanical stability against particle overlap

$$V_{rep}(r, b) = \begin{cases} 4\epsilon \left[ \left( \frac{b}{r} \right)^{12} - \left( \frac{b}{r} \right)^6 + \frac{1}{4} \right] & r \leq r_c \\ 0 & r > r_c, \end{cases} \quad (1)$$

with  $r_c = 2^{1/6}b$ .  $\epsilon$  defines the unit of energy. An effective cylindrical lipid shape is achieved by choosing  $b_{head,head} = b_{head,tail} = 0.95 \sigma$  and  $b_{tail,tail} = \sigma$ , where  $\sigma$  is the unit of length. The three beads are linked by two harmonic bonds,

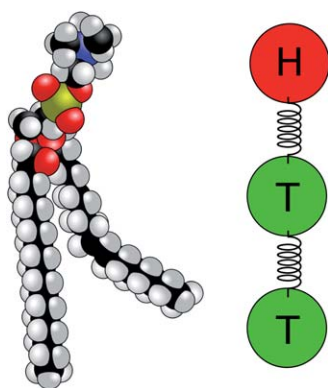


**Fig. 1** An example of a common phospholipid (dipalmitoylphosphatidylcholine, DPPC, chemical formula  $C_{40}H_{80}NO_8P$ ) and its coarse grained representation. The CG model is composed of three parts, one hydrophilic head (H) bead and two hydrophobic tail (T) beads, connected by harmonic bonds.

$$V_{bond}(r) = -\frac{1}{2}k_{bond}(r - \sigma)^2, \quad (2)$$

with stiffness  $k_{bond} = 500\epsilon\sigma^2$ . Lipids are straightened by a harmonic spring with rest length  $4\sigma$  between head and second tail bead

$$V_{bend}(r) = \frac{1}{2}k_{bend}(r - 4\sigma)^2, \quad (3)$$

with  $k_{bend} = 10\epsilon\sigma^2$ . Finally, all *tail* beads interact according to

$$V_{att}(r) = \begin{cases} -\epsilon & r < r_c \\ -\epsilon \left[ \cos \frac{\pi(r - r_c)}{2w_c} \right]^2 & r_c \leq r \leq r_c + w_c \\ 0 & r > r_c + w_c \end{cases} \quad (4)$$

which describes an attractive potential with a depth of  $\epsilon$  which for  $r > r_c$  smoothly tapers to zero. Its decay range  $w_c$  has direct influence on bending rigidity and rupture strength of the membrane, which can be conveniently exploited to simulate lipid bilayers with a broad range of mechanical properties. While this model was originally intended to describe stable fluid bilayers *without the need for additional solvent*, we explicitly model the aqueous environment as it serves as the medium for shock wave propagation. The additional pressure due to the solvent affects the range over which  $w_c$  gives rise to stable bilayers:  $w_c$  needs to be reduced for solvated membranes, compared to the original model.

A major computational bottleneck for all-atom simulations of lipid membranes including electrostatics is caused by the expensive Coulombic interactions of the many water molecules required for sufficient solvation. Therefore, we chose to model water with a recently published CG model,<sup>23</sup> which is based on a short-ranged Morse potential:

$$V_{H_2O}(r) = \begin{cases} A\epsilon \left[ e^{\alpha \left( 1 - \frac{r}{\sigma} \right)} - 2e^{\frac{1}{2}\alpha \left( 1 - \frac{r}{\sigma} \right)} \right] & r \leq r_{c,H_2O} \\ 0 & r > r_{c,H_2O} \end{cases} \quad (5)$$

with  $\alpha = 7$ ,  $A = 1.31911$ , and  $r_{c,H_2O} = 2.544\sigma$ . One water bead represents four  $H_2O$  molecules. This coarse grained potential

reproduces the heat of vaporization, surface tension and compressibility of water with good accuracy. The interaction of membrane head particles with water beads is also given by eqn (5), while the hydrophobic lipid tail particles repel water particles according to eqn (1) with  $b = 1$ . Mapping to real units is achieved by specifying  $\epsilon = 310\text{ K} \times k_B$  and  $\sigma = 0.629\text{ nm}$ . Particle masses are chosen as  $m_{H_2O} = 72\text{ g mol}^{-1}$ ,  $m_{tail} = 115\text{ g mol}^{-1}$ , and  $m_{head} = 220\text{ g mol}^{-1}$ , which yields a reasonably realistic mass density profile of the solvated lipid bilayer, as will be detailed below.

## 2.2 Shock-wave generation

Shock waves were initiated with a momentum reflecting mirror,<sup>24</sup> a standard method for generating shock waves in simulation studies of hard condensed matter. Here, a piston of infinite mass moves with constant velocity  $v_p$  against the target material. All particles coming into contact with the piston surface are specularly reflected. This method is quite similar to standard shock wave experiments, where a static target material is hit by a fast-moving impactor.<sup>25</sup> Upon impact, the target material is compressed and the resulting steep density gradient initiates a shock wave. This method allows for producing fast shock-waves up to  $10000\text{ ms}^{-1}$  with a well defined shock-wave front and good numerical stability. An alternative method was used by Kobayashi *et al.*,<sup>12</sup> who added a constant hypersonic velocity to all particles enclosed within a certain region of the simulation volume. The latter method is computationally less efficient compared to the momentum reflecting mirror as a comparatively larger number of particles is required for initiating the shock-wave.

## 2.3 Dissipative particle dynamics with conserved energy

In DPD,<sup>18,19</sup> atomistic representations are reduced to models with only a small number of particles, and the “fast” variables related to the coarse-grained (integrated out) degrees of freedom are replaced by random and dissipative forces, which mimic thermal fluctuations. Because these interactions only control temperature and dynamics, conservative forces  $\mathbf{F}_{ij}^C$  derived from the interaction potentials as discussed in Section 2.1 need to be included in order to lend structure to the system. The random and dissipative interactions between particles  $i$  and  $j$  read<sup>26</sup>

$$\mathbf{F}_{ij}^R = \zeta \omega^R(r_{ij}) \mathbf{e}_{ij} \frac{\xi_{ij}}{\sqrt{\delta t}} \quad (6)$$

$$\mathbf{F}_{ij}^D = -\gamma \omega^D(r_{ij}) (\mathbf{v}_{ij} \cdot \mathbf{e}_{ij}) \mathbf{e}_{ij}, \quad (7)$$

where  $\mathbf{r}_{ij} = \mathbf{r}_i - \mathbf{r}_j$ ,  $r_{ij} = |\mathbf{r}_{ij}|$ ,  $\mathbf{e}_{ij} = \mathbf{r}_{ij}/r_{ij}$ , and  $\mathbf{v}_{ij} = \mathbf{v}_i - \mathbf{v}_j$ , with  $\mathbf{r}$  and  $\mathbf{v}$  being the particle's position and velocity, respectively. The  $\xi_{ij}$  are symmetric random variables with zero mean and unit variance, which are independent for different pairs of particles and different times.  $\omega^D(r_{ij})$  and  $\omega^R(r_{ij})$  are weight functions with typically compact support, determining the DPD interaction radius between two particles. A fluctuation-dissipation theorem relates these functions, as well as the amplitudes  $\zeta$  and  $\gamma$  of the random and viscous dissipative forces, in order to preserve the canonical phase space measure:

$$\omega^D(r_{ij}) = [\omega^R(r_{ij})]^2 \quad (8)$$

$$\gamma = \frac{1}{2k_B T} \zeta^2 \quad (9)$$

We employ the standard linear DPD weight function with interaction range  $r_{c,DPD}$ ,

$$\omega^R(r_{ij}) = \begin{cases} 1 - r_{ij}/r_{c,DPD} & r_{ij} \leq r_{c,DPD} \\ 0 & r_{ij} > r_{c,DPD} \end{cases} \quad (10)$$

$\zeta$  is a free parameter which controls the amount of momentum exchange between pairs of particles per time step and has direct influence on the dynamics of the system. We determine  $\zeta$  such that the here employed CG water model reproduces the kinetic energy dissipation profile of an atomistic simulation of SPC water, as will be detailed in Sec. 3. With the above definitions, the DPD equations of motion read:

$$d\mathbf{r}_i = \mathbf{v}_i dt \quad (11)$$

$$d\mathbf{v}_i = \frac{1}{m_i} \left[ \sum_{j \neq i} (\mathbf{F}_{ij}^C + \mathbf{F}_{ij}^D + \mathbf{F}_{ij}^R) \right] dt. \quad (12)$$

Up to this point, the temperature is fixed in the fluctuation-dissipation theorem, eqn<sup>9</sup>, with the effect that DPD is actually a thermostat, which adds to, and removes energy from the system, until the particles' kinetic energy is in agreement with the specified temperature. This behavior is not desired when temperature gradients need to be simulated. In this case, it is necessary to consider a DPDE model, where the fluctuation-dissipation theorem is not fixed *a priori*, but evolves depending on the physical events that have happened.<sup>17</sup> DPDE with conserved energy (DPDE),<sup>20,21</sup> addresses this issue. In DPDE, an internal energy reservoir  $\varepsilon_i$  is attached to each particle, which represents internal degrees of freedom. The variation of the total mechanical energy through the random and dissipative forces are compensated by adding or removing energy from the internal reservoirs, such that the total energy remains constant. The temperature for each particle is obtained by specifying a heat capacity function  $C_{v,i}(\varepsilon_i)$  for each particle. Here, we assume that the internal degrees of freedom are purely harmonic, such that  $C_{v,i} = N_{F,i} k_B$ , with  $N_{F,i}$  equalling the number of degrees of freedom of those atoms which a CG bead represents. The internal temperature is then given by  $T_i = \varepsilon_i / N_{F,i} k_B$ . In DPDE, the fluctuation-dissipation relation eqn<sup>9</sup> depends on a *local* temperature, computed for each pair of particles individually,

$$\gamma_{ij} = \frac{1}{2k_B T_{ij}} \zeta^2, \quad (13)$$

where  $T_{ij} = 2 \left( \frac{1}{T_i} + \frac{1}{T_j} \right)^{-1}$ . As a result, the momentum exchange between particles, effected by the random and dissipative forces, depends now on their internal temperature. DPDE assumes that this momentum exchange determines the variation of the particles' internal energy  $\varepsilon_i$  such that the total energy (the sum of kinetic, potential, and internal energy) is conserved. Obtaining an equation of motion which governs the variation of the internal energy from the latter requirement is somewhat involved, as one needs to take the stochastic nature of the dissipative process into account. We quote here the final result, which has been obtained using Itô calculus:<sup>21</sup>

$$d\varepsilon_i = \frac{1}{2} \sum_{j \neq i} \left[ \gamma_{ij} \omega^D(r_{ij}) (\mathbf{v}_{ij} \cdot \mathbf{e}_{ij})^2 - \frac{\zeta^2}{2} \left( \frac{1}{m_i} + \frac{1}{m_j} \right) \omega^D(r_{ij}) - \zeta \omega^R(r_{ij}) (\mathbf{v}_{ij} \cdot \mathbf{e}_{ij}) \frac{\xi_{ij}}{\sqrt{\delta t}} \right] dt \quad (14)$$

We note here that the original derivations of DPDE also include macroscopic thermal conduction. However, following the arguments presented by Stoltz,<sup>17</sup> we neglect these terms here as the evolution of the internal energies is expected to be dominated by dissipative forces at the shock front. Additionally, as the individual mesoscopic particles considered here only represent approximately 10 to 50 atoms, we expect macroscopic heat diffusion processes to be realistically modeled by momentum exchange only.

## 2.4 Computer programs and implementation details

The results presented in this article have been generated with a number of different simulation codes. All-atom simulations of a DPPC membrane solvated in SPC water, as well as SPC water itself, were conducted with the MD package Gromacs<sup>27</sup> using Particle-Mesh-Ewald electrostatics. Equilibrium properties of our CG model were obtained using the MD package LAMMPS.<sup>28</sup> Here, preassembled solvated membrane configurations were carefully equilibrated using Langevin dynamics with a time step  $\delta t = 33.25$  fs and a Berendsen barostat to temperature  $T = 310$  K and pressure  $p = 1$  atm. Shock wave simulations using the DPDE equations of motion were performed with our own code, based on the excellent examples of Rapaport.<sup>10</sup> These simulations were started from equilibrated structures using a shorter time step  $\delta t = 2.87$  fs, which, together with a Velocity-Verlet integrator, resulted in good energy conservation. The required heat capacities, which relate internal energy and temperature in the DPDE scheme, were taken as follows: One CG water bead represents four water molecules, corresponding to a total number of degrees of freedom (DOF)  $N_F = 36$ . For each DOF, we assume a purely harmonic relationship for both potential and kinetic energy, resulting in a heat capacity  $C_V = 36 k_B$ . A DPDE water bead has three independent translational DOF, resulting in an internal heat capacity of  $C_V = 33 k_B$ . A similar procedure applies to the lipid beads; in this case we use the DPPC example lipid to obtain a total  $N_F^{DPPC} = 390$ . However, the mass density of the CG lipids vs. the DPPC lipids also needs to be considered: As one CG lipid weighs only 450 g mol<sup>-1</sup>, and one DPPC lipid 734 g mol<sup>-1</sup>, the effective CG number of DOF has to be scaled accordingly, resulting in  $N_F^{CG} \approx 239$ . Distributing these evenly over the CG lipid, and subtracting three DOF for the translational motion of each bead, we finally have  $C_V \approx 77 k_B$  per lipid bead. The DPDE interaction cutoff was set to  $r_{c,DPD} = 1.6$  nm.

## 3 Results

### 3.1 Lipid bilayer equilibrium properties

We begin this section by demonstrating that our CG model reproduces key mechanical properties of real lipid bilayers.

**3.1.1 Lipid bilayer stability.** The attractive range of the lipid tail interactions is governed by the decay range  $w_c$ , as discussed



above. We find stable bilayer structures in the interval  $w_c = [0.8\sigma, 1.4\sigma]$  at a temperature  $T = 310$  K, which corresponds to physiological conditions. For  $w_c \leq 0.7\sigma$ , the bilayer dissolves, while it is crystalline for  $w_c \geq 1.5\sigma$ . The fluid character of the bilayer within the stable range is verified by computing the in-plane diffusion coefficient  $D = 0.03 - 0.06\sigma^2/\tau$  and observing a non-zero flip-flop rate, *i.e.*, the probability per unit time that a single lipid changes from one leaflet to the other.

**3.1.2 Mass density distribution.** During shock wave impact, the lipid bilayer is subjected to great forces, leading to strong accelerations. This suggests that it is imperative for the CG model to have a realistic mass distribution in order to correctly account for inertial effects. Fig. 2 compares the CG model mass density distribution, measured along the direction normal to the bilayer plane, with the results of an all-atom simulation of dipalmitoylphosphatidylcholine (DPPC), a common phospholipid in eucaryotic cells. The agreement is quite satisfactory with the density peaks at the hydrophilic head groups and the depletion zone at the bilayer center being well reproduced. In order to study the inertial effects during shock-wave impact in more detail, we also consider the situation, where the masses of the CG phospholipid beads are chosen such as to reproduce a uniform density profile, *i.e.*, as situation where the phospholipid bilayer has the same mass density as water.

**3.1.3 Elastic moduli.** The bending elasticity modulus  $\kappa$  determines by how much an applied external force deforms a lipid bilayer from its perfectly flat energetic ground state. It can be obtained from linear response theory by analyzing the bilayer height fluctuation spectrum. Helfrich's linearized continuum theory<sup>29</sup> predicts the following relation for a two-dimensional elastic sheet:

$$S(n) = \langle c_n c_n^* \rangle = \frac{k_B T L_{\parallel}^2}{16\pi^4 (\kappa n^4 + s n^2)}, \quad (15)$$

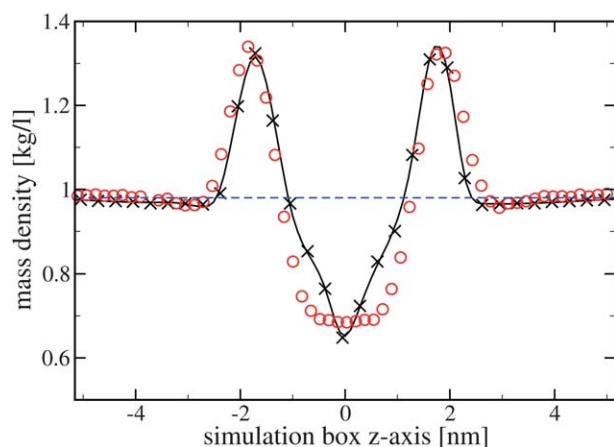


**Fig. 2** Mass density distributions, measured along the direction normal to the bilayer planes, of the common membrane phospholipid DPPC (black crosses and line), and the here employed generic CG model (red circles). The blue dashed line represents the artificial uniform density profile, which is also studied in order to further elucidate inertial effects during shock-wave impact.

where

$$c_n = \frac{1}{N} \sum_{j=1}^N (z_j - z_0) \exp \left[ \frac{-2\pi i}{L_{\parallel}} (n_x x_j + n_y y_j) \right] \quad (16)$$

is a Fourier component of the deviation of the local bilayer height with respect to from its average height  $z_0$ . The sum runs over all bilayer particles with coordinates  $x_j, y_j$ , and  $z_j$ .  $\mathbf{n}$  is a two-dimensional vector with components  $n_x$  and  $n_y$  in reciprocal space, which relates to a wave-vector through  $\mathbf{q} = 2\pi\mathbf{n}/L_{\parallel}$ .  $s = L_{\perp}(2p_{zz} - p_{xx} - p_{yy})$  is the surface tension, which is related to the diagonal components of the pressure tensor  $p_{\alpha\beta}$ . As we perform NPT MD simulations for the equilibrium properties, the pressure is isotropic with  $p_{zz} = p_{xx} = p_{yy}$ , such that the surface tension vanishes. Expressing eqn (15) in terms of wave-vectors, we obtain  $S(q) \propto q^{-4}$ . However, this expression is only valid in the regime below the crossover wave-vector  $q = \sqrt{\sigma/\kappa}$ , as  $S(q)$  probes the internal structure of the lipid bilayer at higher wave-vectors. We simulated systems with 3872 lipids and  $L_{\parallel} \approx 29$  nm, depending on the value of  $w_c$ . As shown in Fig. 3, the asymptotic  $q^{-4}$  scaling regime is recovered at this system size, which implies that the characteristic lipid bilayer bending modes can be accommodated in the simulation box. We obtained the bending rigidities by fitting eqn (15) to the simulation data. Continuum theory relates<sup>30</sup>  $\kappa$  to the area compression modulus *via*  $K_A = 24\kappa/d^2$ , with  $d$  being the bilayer thickness, which we take to be 5 nm (*cf.* Fig. 2). Results for these quantities are given in Table 1. We note that the values obtained from our simulations are well within the experimental<sup>30,31</sup> range, which is  $K_A \approx 234$  mN m<sup>-1</sup>, and  $\kappa = 10\text{--}40 k_B T$ , depending on the technique used, such as micropipet aspiration or various forms of optical measurements.

## 3.2 Effects of shock wave impact.

**3.2.1 Parametrization of the DPDE dissipation rate.** The parameter  $\zeta$  appearing in the DPDE integration scheme, eqn (6) is used to adjust the conversion rate of ordered kinetic energy into random thermal motion. We choose  $\zeta$  such that the kinetic energy relaxation profile of our CG model of water reproduces

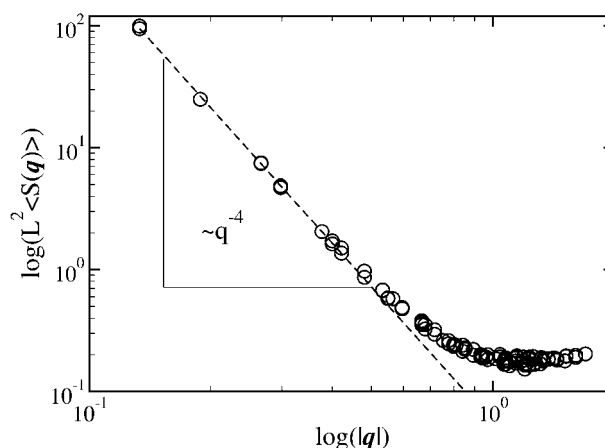


**Fig. 3** Membrane height fluctuation spectrum for a bilayer system with 3872 lipids, interacting with attraction parameter  $w_c = 1\sigma$ . Scaling of the spectrum follows the relation  $S(q) \propto q^{-4}$ , as predicted by continuum theory.

**Table 1** Bending stiffness  $\kappa$ , compression modulus  $K_A$ , and simulation box size  $L_{\parallel}$  for bilayers with different stability lipid attraction parameters  $w_c$ .

$w_c/\sigma$	$\kappa/k_B T$	$K_A/mN$	$L_{\parallel}/nm$
0.8	$13.7 \pm 0.5$	$142 \pm 5$	$29.62 \pm 0.01$
1.0	$14.6 \pm 0.6$	$152 \pm 6$	$29.27 \pm 0.01$
1.2	$16.3 \pm 0.5$	$169 \pm 5$	$28.38 \pm 0.01$
1.4	$22.6 \pm 0.8$	$235 \pm 8$	$27.16 \pm 0.05$

the results obtained from an atomistic simulation of  $H_2O$ , using the fully flexible SPC model.<sup>32</sup> Both CG and SPC simulations were started from configurations of size  $(7.1 \times 7.1 \times 14.2) \text{ nm}^3$ , equilibrated at 1 atm and 310 K. The shock was generated by setting the z-component of the particles' velocity to  $4000 \text{ ms}^{-1}$ , for those particles located in a slab of width 2 nm, parallel to the  $xy$ -plane. Fig. 4 shows that  $\zeta$  has substantial influence on the relaxation profile. While the exemplary values  $\zeta = 0.5$  and  $\zeta = 0.001$  (in reduced units) lead to too fast and too slow relaxation rates, respectively, we find reasonable agreement between CG and SPC simulations at  $\zeta = 0.09375$ . It is appropriate to remark that  $\zeta$  directly affects the viscosity,<sup>20</sup> but rather than adjusting the viscosity of the CG water model to match that of real water, we chose to parametrize the kinetic energy dissipation, as temperature effects appear to be more important for the small stable range of phospholipid bilayers in the phase diagram.

**3.2.2 Evolution of the shock wave front.** Using the DPDE dissipation rate as motivated above, we performed shock wave experiments on square lipid bilayer patches for values of the lipid interaction parameter in the interval  $w_c \in [0.8\sigma, 1.4\sigma]$ . For  $w_c \leq 0.7\sigma$ , the bilayer dissolves, while it is crystalline for  $w_c \geq 1.5\sigma$ . Thus, the investigated range is representative of a wide spectrum of lipid bilayers with different mechanical stability. Initial configurations were taken from equilibrium runs performed in

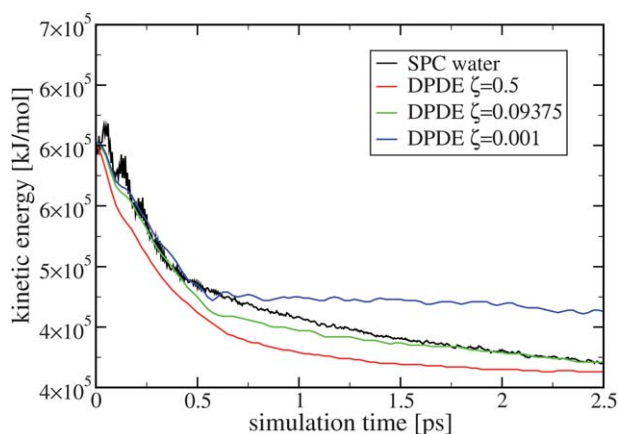


**Fig. 4** Influence of the free DPDE parameter  $\zeta$  on the kinetic energy dissipation of a shock-wave. The reference is an all-atom simulation of SPC water; for comparison DPDE results using the coarse-grained model of water, eqn (5), are shown.

the tensionless state. Two system sizes were considered: a smaller system with 1058 lipids and a larger system with 3872 lipids, with  $L_{\parallel} \approx 15 \text{ nm}$  and  $L_{\parallel} \approx 30 \text{ nm}$  in the tensionless state, respectively. The simulation box size along the direction normal to the bilayer was chosen as  $L_{\perp} = 63.08 \text{ nm}$  in both cases, in order to allow for comparing both system sizes. The total number of particles including water beads amounted to roughly 500 000 and 120 000 for the larger and smaller systems, respectively. Shock waves in these systems were generated with a momentum-reflecting mirror as described in Section 2.2, with the piston moving parallel to  $L_{\perp}$ . The driving speed of the piston was varied in the range  $v_p \in [1892 \text{ ms}^{-1}, 5676 \text{ ms}^{-1}]$  in order to produce shock waves with different supersonic velocities. After 200 time steps of  $\delta t = 2.87 \text{ fs}$ , the piston was stopped, while the initiated shock wave continued to travel further along  $L_{\perp}$ . The lipid bilayer was placed 9.435 nm in front of the initial piston position, far enough away not to be hit by the piston. Snapshots of an exemplary simulation are shown in Fig. 5, where the shock-wave was initiated by a piston with velocity  $v_p = 4730 \text{ ms}^{-1}$ . Visual inspection of the lipid bilayers after shock-wave impact (cf. Fig. 6) shows that the here considered range of shock front speeds causes little to heavy damage to the equilibrium bilayer structure.

For a complete analysis of shock-wave experiments, it is desirable to follow the shock wave front velocity and peak pressure, as it travels through the simulation box and dissipates. Consequently, we discretize the simulation volume in thin slabs of width 0.5 nm which are oriented parallel to the  $xy$ -plane. By computing the average velocity and pressure in each slab for each simulation timestep individually, the evolution of the shock-wave front can be studied in detail. The pressure profiles corresponding to the same system as displayed in Fig. 5 are shown in Fig. 7: at  $t = 0 \text{ ps}$ , one can identify the location of the lipid bilayer by the interfacial pressure variations near  $z \approx 9.4 \text{ nm}$ . The profiles at  $t = 0.43 \text{ ps}$  and  $t = 12.49 \text{ ps}$  clearly show the shock-wave front with an associated pressure peak. The fast dissipation of the shock-wave is demonstrated by the quickly diminishing peak pressure heights. The minor pressure peak near  $z \approx 20 \text{ nm}$  in the  $t = 12.5 \text{ ps}$  profile is due to the phospholipid bilayer, which has moved to the right during the simulation, as the compressing piston introduces a finite linear momentum.

In order to determine the speed of the shock-wave, we identified the  $z$ -location of the shock-wave front,  $l_s(t)$ , as a function of simulation time. A simple linear function, which describes the attenuation from the hypersonic velocity to constant sound speed was then fitted to these location data:

$$l_s(t) = \frac{at}{t+b} + ct. \quad (17)$$

This saturation-like function fits the recorded data very well, with the fitted value of  $c$  being close to the sound speed of the medium, as is physically required. The speed of the shock wave front is given by the derivative of  $l_s(t)$  with respect to time,

$$v_s(t) = \frac{d}{dt} l_s(t) = \frac{a}{b+t} - \frac{at}{(b+t)^2} + c. \quad (18)$$

For our purposes, it is of interest to know the speed of the shock wave front,  $v_s$ , as it impacts the phospholipid bilayer. Because the precise location of the bilayer is known, the time of impact is

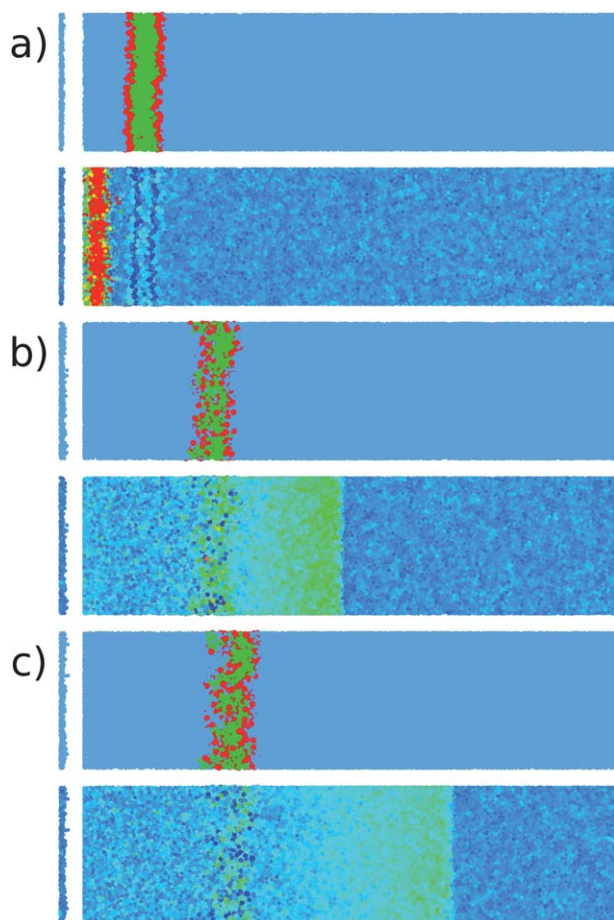


**Fig. 5** Snapshots of a shock wave experiment with a lipid bilayer (interaction parameter  $w_c = 1 \sigma$ ) at different times. The simulation box measures  $(62.90 \times 15.01 \times 15.01) \text{ nm}^3$ , comprising 117 556 particles. A piston, coming from the left and moving with a velocity of  $4730 \text{ ms}^{-1}$ , compresses the material ahead of it and induces a shock wave. The compression leaves a void visible near the left edge of every snapshot. Part (a), (b), and (c) correspond to simulation times of 0.72 ps, 8.61 ps, and 14.36 ps, respectively. For each part the same snapshot is shown twice: in the upper snapshots, particles are colored according to type (blue – water, red – lipid head, green – lipid tail). In the lower snapshots, the pressure distribution is shown, with blue and red signifying low and high pressure, respectively. Peak pressures in (a), (b), and (c) are 38.4 GPa, 3.0 GPa, and 1.9 GPa, respectively. The lipid bilayer is moved to the right during the simulation, as the compressing piston introduces a finite linear momentum in the compression direction.

given by solving eqn (17) for  $t$ , and calculating the impact velocity from eqn (18). This approach has the advantage that it yields an analytic expression for the velocities. Calculating the velocity directly from finite time differences of the location data is not a viable alternative due to numerical noise. Fig. 8 shows the thus obtained velocities as a function of distance from the compressing piston. It is clear from this graph, that attenuation of the shock-wave front velocity proceeds very quickly, in agreement with experiment.<sup>33</sup>

### 3.2.3 Membrane order parameters and shock wave induced damage.

There are a number of different phenomena associated

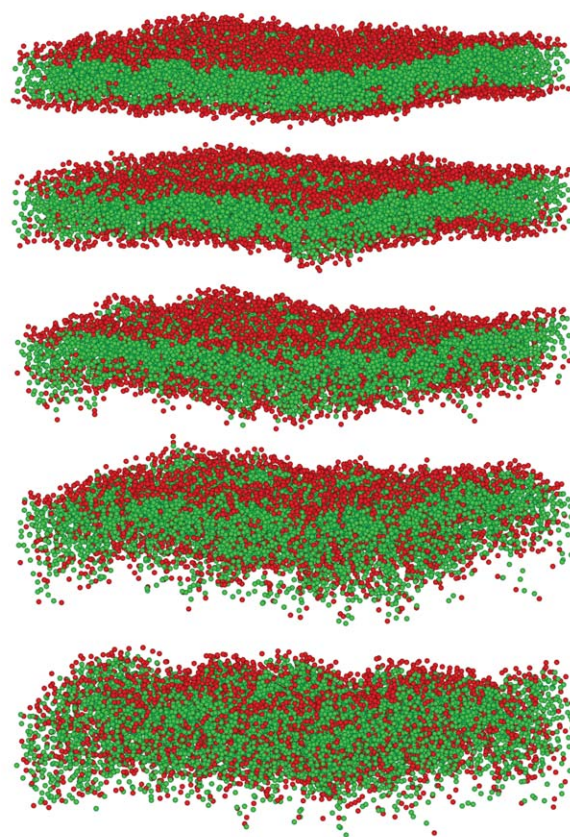


**Fig. 6** Lipid bilayer damage induced by shock waves. Snapshots are shown for a system with  $L_{||} = 29.3 \text{ nm}$ , comprising 3872 lipids with interaction parameter  $w_c = 1.0 \sigma$ , 25 ps after shock wave impact. Water beads have been left out for better visualization of the bilayer. The shock front velocity at impact varies from top to bottom as  $v_s = 2107 \text{ ms}^{-1}$ ,  $2956 \text{ ms}^{-1}$ ,  $3897 \text{ ms}^{-1}$ ,  $5090 \text{ ms}^{-1}$ , and  $6666 \text{ ms}^{-1}$ .

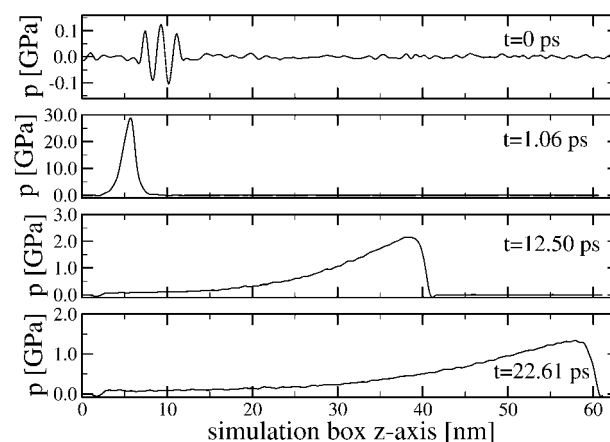


**Fig. 7** Pressure profiles at different times resulting from an initial piston velocity of  $4730 \text{ ms}^{-1}$ . The system is the same as described in Fig. 5. Note the different ordinate scales.

with lipid bilayer damage: (i) the bilayer can tear along well localized paths leaving the majority of its area intact, (ii) the two bilayer leaflets can interpenetrate upon compression, (iii) and single lipids can move out of their equilibrium positions and



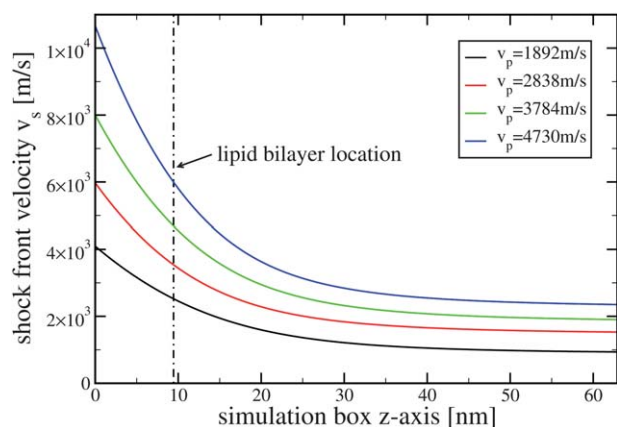


**Fig. 8** Evolution of the shock front velocity  $v_s$  for different driving speeds  $v_p$  of the momentum reflecting mirror. The dashed line shows the location of the lipid bilayer at  $z = 9.435$  nm.

orientations *via* diffusive mechanisms. We take a pragmatic approach to combine all of these effects into a single scalar order parameter,  $\Psi$ , which is based on the projection of the particle pair distribution function on rotational invariants.<sup>34</sup> To do so, we define the orientation dependent correlation function

$$O(r) = \frac{\sum_{i>j}^N \delta(r - r_{ij}) \mathbf{e}_i \cdot \mathbf{e}_j}{4\pi N r^2}, \quad (19)$$

where the sum runs over all pairs of lipids  $i$  and  $j$ ,  $r_{ij}$  is the pair distance as measured between the central beads,  $\delta$  is the Dirac Delta distribution, and  $\mathbf{e}_i$  and  $\mathbf{e}_j$  are orientation vectors (the normalized distance vectors between the first and the third bead of each lipid).  $O(r)$  is similar to the familiar radial distribution function, except that it is additionally weighted by relative orientations. To convert this distance dependent correlation function into a single scalar, we integrate  $O(r)$  up to a distance  $r_c = 1.0$  nm, which is chosen such as to include the first coordination shell, *i.e.*, the first peak in  $O(r)$ , in the undamaged bilayer structure.

$$\Psi = 4\pi \int_0^{r_c} O(r) r^2 dr \quad (20)$$

Disruption of the equilibrium bilayer configuration affects this order parameter in two different ways: If the mutual orientation of neighboring lipids deviates from parallel alignment, or if lipids are separated from each other beyond their equilibrium distance  $r_c$ , the value of  $\Psi$  is reduced, thus providing a quantitative means to characterize lipid bilayer damage.

In addition to the above introduced order parameter, we also consider the variance of the bilayer height:

$$\Lambda = \frac{1}{N} \left\{ \sum_{i=1}^N [\delta z_i(t)]^2 - \sum_{i=1}^N [\delta z_i(0)]^2 \right\} \quad (21)$$

Here,  $\delta z_i(t) = z_i(t) - \frac{1}{N} \sum_{i=1}^N z_i(t)$  is the momentary deviation of the  $z$ -coordinate of particle  $i$  from the average bilayer  $z$ -position, and  $\delta z_i(0)$  is the corresponding value of the equilibrated structure at the start of the simulation.  $\Lambda$  is a measure for the width of the

bilayer thickness distribution and captures the initial compression due to the shock-wave impact as well as the surface roughening associated with diffusive disintegration of the membrane.

**3.2.4 Effects of system size and shock-wave speed.** We justify our choice of system size – 3872 lipids, with a lateral length  $L_{\parallel} \approx 30$  nm – by noting that it is large enough to capture the characteristic bilayer undulations, which are driven by thermal fluctuations. This is verified in Fig. 3, where the Fourier transform of the lipid bilayer height fluctuations reach the asymptotic scaling regime predicted by continuum theory. We therefore assume that such a lipid bilayer patch is a representative element, such that the periodic boundary conditions do not introduce large artificial errors. Fig. 9 shows the damage caused by shock-waves of different impact velocities  $v_s$ , as measured by the order parameter  $\Psi$ . The lipid bilayer was chosen to be of medium stability, with an interaction parameter  $w_c = 1 \sigma$ . A clear trend emerges from the result, with higher impact velocities causing a stronger decrease of  $\Psi$ . The initial steep decrease in  $\Psi$  is almost instantaneous for all shock-wave speeds considered, however, the following behavior is dependent on  $v_s$ : for  $v_s \leq 3000$  ms<sup>-1</sup>,  $\Psi$  increases within a few ps, indicating reversible damage. For  $v_s \geq 3920$  ms<sup>-1</sup>, no such recovery can be observed. This analysis is supported by considering the measure  $\Lambda$ , see Fig. 10, which displays the bilayer height variance. Here, the result for  $v_s = 2140$  ms<sup>-1</sup> shows very clearly a reversible compression and extension cycle, whereas the simulations with and  $v_s \geq 3920$  ms<sup>-1</sup> suggest a continuous (on the time-scale of the simulation) increase of the membrane thickness. The origin of this increase is associated with diffusive disintegration and surface roughening, as evidenced by the snapshots shown in Fig. 6 and Fig. 11. These results are obviously limited by the timescale available for studying the long-time behavior of  $\Psi$  and  $\Lambda$ . However, we note that with real cell membranes, the short time behavior is crucial as the turgor pressure within the cell is usually higher than that of

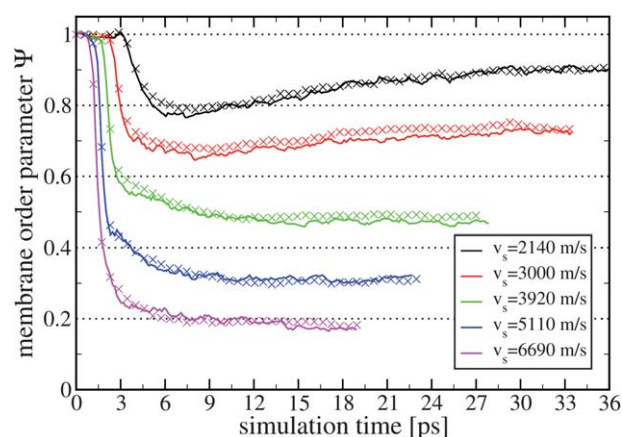


**Fig. 9** Membrane damage induced by shock waves of different incident velocities  $v_s$ . The data shown are for the CG lipid model with interaction parameter  $w_c = 1 \sigma$  and two different system sizes: Lines and crosses are for bilayers with 1082 and 3872 lipids, respectively. The data points for faster  $v_s$  extend to shorter times than those for slower  $v_s$ , as the simulation box size is fixed and a faster shock-wave takes less time to traverse the box.

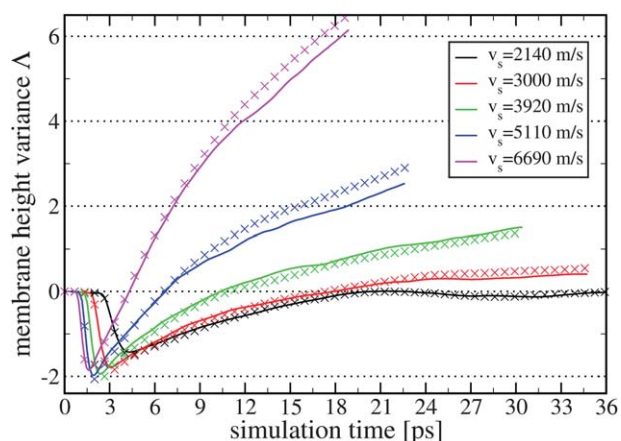


**Fig. 10** Membrane damage induced by shock waves of different incident velocities  $v_s$ . Systems and symbols are the same as for Fig. 9, but here the variance of the bilayer height is shown.

its surroundings, which means that a cell, once sufficiently ruptured, will quickly drain. We note that the two system sizes considered here show no significant difference in the resulting

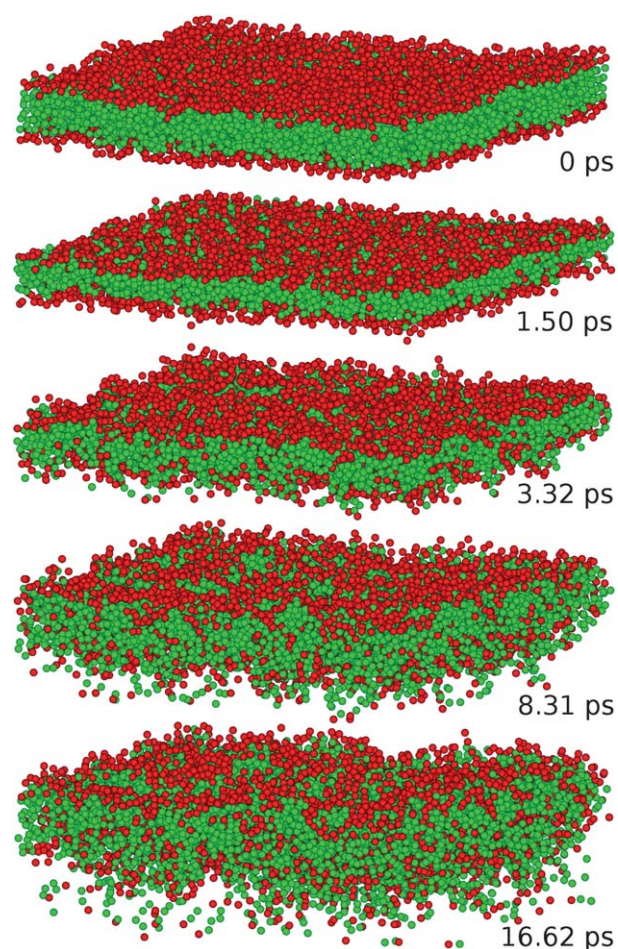


**Fig. 11** Trajectory snapshots of a system with 3872 lipids and interaction parameter  $w_c = 1.0 \sigma$  depicting the compression and diffusive disintegration phases caused by a fast shock-wave with an impact velocity of  $6666 \text{ ms}^{-1}$ . The time values next to each configuration correspond to the elapsed simulation time.

variation of the order parameters. Hence, we conclude that these system sizes are already large enough to study simple aggregate order parameters such as  $\Psi$  and  $\Delta$ , which are computed by averaging over one configuration.

**3.2.5 Effects of bilayer stability and inertia.** As detailed above, the CG model used here is capable of simulating lipid bilayers of different stability, ranging from unstable bilayers close to the mixing transition to almost solid bilayers, close to the crystallization transition. We exploit this feature in order to study the relation of bilayer stability and shock-wave induced damage. Fig. 12 compares the variation of  $\Psi$  for these two bilayers with  $w_c = 0.8 \sigma$  and  $w_c = 1.4 \sigma$ , which are representative of the extreme ends of the stable bilayer range. The graph shows a clear difference in the resulting damage of these two systems, however, it is surprising that bilayer stability has such a quantitatively small effect, especially at long times after shock-wave impact. A possible explanation for this result is that the difference in cohesive energy density between these two systems is smaller by orders of magnitude than the energy densities introduced temporarily by the shock-wave.

This observation motivates another experiment, which aims at investigating the importance of inertial effects on the induced damage. During shock-wave impact, particles are subjected to strong acceleration, which is affected by their moment of inertia. To test for such inertial effects, we compare the variation of  $\Psi$  for lipid bilayers with the different mass density distributions as discussed in Sec. 3.1. The results are shown in Fig. 13, where no significant difference in damage can be identified between the realistic and artificial uniform mass density profiles. We thus conclude that inertial effects are negligible for the damage mechanism occurring in the interaction of lipid bilayers with shock waves.

## 4 Conclusions

In this paper, we have presented computer experiments on the interaction of shock-waves with coarse-grained models of lipid

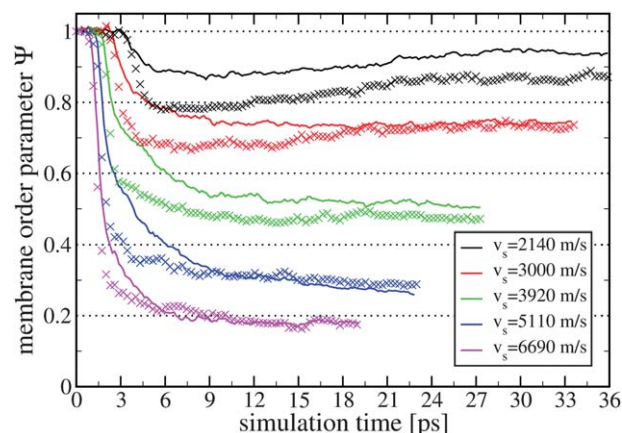


**Fig. 12** Effect of lipid attraction parameter  $w_c$  on bilayer damage induced by shock waves of different incident velocities  $v_s$ . Lines show results for the CG lipid model with interaction parameter  $w_c = 1.4 \sigma$ , being representative of a very stable lipid bilayer. Crosses show the induced damage for lipids with  $w_c = 0.8 \sigma$ , which is close to the lower end of the stable bilayer regime in the phase diagram.



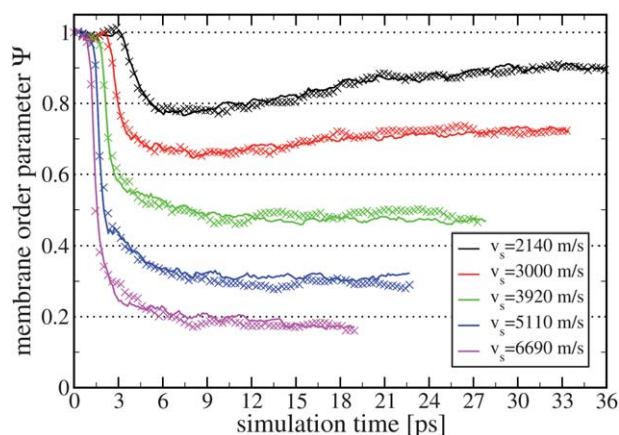


**Fig. 13** Effect of mass density distribution on bilayer damage induced by shock waves of different incident velocities  $v_s$ . Lines show results for the CG lipid model with a realistic mass density profile, while crosses show results for the artificial uniform profile.

bilayers, which are the dominant constituents of the plasma membrane and the endomembrane in eukaryotic cells. Our model, which represents an entire lipid molecule with only three beads, aims at computational efficiency rather than capturing molecular detail. This way, we can simulate larger systems with reasonable CPU time than what is currently possible with atomistic MD simulations. Our simplified model successfully reproduces key mechanical properties of real lipid bilayers such as the bending rigidity, the fluid character, and the area compression modulus. The lack of molecular detail is of particular advantage to this study, as it aims to elucidate the basic damage mechanisms when a soft structure such as a lipid bilayer is impacted by a shock-wave.

We have studied lipid bilayer patches of lateral size  $L_{\parallel} \approx 30$  nm. This system size is large enough to accommodate the characteristic bilayer bending modes, which can be considered a minimum requirement in order to rule out finite-size effects. This system size, together with the large amount of water required to model the aqueous environment would have required enormous computational resources if full atomistic molecular dynamics had been used instead of our CG description. The here employed DPDE technique facilitates faithful simulations of non-equilibrium processes such as shock-waves, as it allows to recover the correct heat capacity for coarse-grained models with highly reduced number of degrees of freedom.

The parameter range of the lipid interaction potentials were chosen such that mechanically barely stable bilayers as well as very stable bilayers could be simulated. Therefore, our numerical experiments are representative of a wide range of different real phospholipid bilayers. The results of our shock-wave experiments indicate a threshold shock front velocity  $v_s \approx 3000$  ms<sup>-1</sup>, below which the bilayer recovers from shock-wave induced damage on the timescale of a few ps. Above this velocity, no such recovery could be observed. Most of the damage is caused instantaneously while the shock-wave front traverses the lipid bilayer, with only little more damage occurring afterwards. A strong correlation between  $v_s$  and the induced damage was observed, however, the dependence of the induced damage on the lipid attraction parameter  $w_c$  was found to be weak. Different

mass distributions within the lipid bilayer were found to have no effect, thus ruling out inertial effects for the damage mechanism.

An explanation for the weak dependence of the attractive lipid interaction parameter on the resistance to shock-wave induced damage is provided by the fact that a lipid bilayer is a liquid, *i.e.*, a phase which is only stable in a very narrow range of the phase diagram. The cohesive energies present in liquids are, in general, on the order of  $k_B T$ , and there is little room to vary the energetic parameters without crossing either the liquid-gas or liquid-solid phase boundary. In the present case, it is the subtle balance between hydrophilic and hydrophobic interactions and the cohesive energy density which enforces a very reduced range of stable fluid lipid bilayers. The shock-wave, in contrast, transiently pumps amounts of energy into the system which exceed  $k_B T$  by orders of magnitude. As a result, little differences in cohesive energy can only play a minor role for the induced damage. The here observed insensitivity of the lipid attraction parameter  $w_c$  with respect to shock-wave response of the bilayer is therefore in accordance with what one expects from fundamental physical considerations.

In comparison with the two existing publications on the interactions of shock-waves with lipid bilayers due to Koshiyama *et al.*,<sup>12,13</sup> which are both detailed all-atom simulations, we note the following points: using a coarse-grained model, we have studied much larger systems with a 21-fold increase in membrane patch area, and an almost 4-fold increase of the simulation box length along the shock impulse direction,  $L_{\perp}$ . This enables us to simulate the bilayer patch in a state which should not be affected significantly by finite-size effects, as the characteristic undulation modes can be accommodated. Additionally, due to the increase in  $L_{\perp}$ , we can study the damage evolution for much longer times: the afore mentioned studies were limited to 600 fs, while we extended this time to 19–36 ps, depending on shock-wave speed. In terms of quantifying the induced damage, Koshiyama *et al.* mainly employed the bilayer thickness, which temporarily decreased during compression, and the Deuterium order parameter,<sup>35</sup> which is an accumulated orientational order parameter similar to eqn (20). Their results for a single DPPC system are qualitatively similar to the results presented here, however, here we have studied a wide range of bilayers of different stability. In addition, we have identified a threshold shock-front velocity below which the induced damage is reversible on the timescale of a few ps. In contrast to detailed all-atom simulations, the merit of the here employed coarse-grained model is simplicity, which helps to understand the general mechanisms of shock-wave and lipid bilayer interaction.

It is a challenge to accurately map the induced damage of a bilayer membrane onto a single number. Here, we have chosen to use a structural correlation, depending on both distance and orientation of individual lipids. This is not necessarily the optimal choice, as this order parameter is essentially an average over an entire bilayer configuration and smooths out singularities such as local rupture. It is also not clear how membrane tension affects the damage behavior, however, we chose to simulate at vanishing tension such that our numerical experiments can be related to existing equilibrium results. In a forthcoming study on the same subject, we will address these issues by simulating much larger planar system which, due to an increase in bilayer area, are expected to show an appreciable number of

singular defects. Also, in order to seek better comparison with real eukaryotic cells, we will report on shock-wave simulations with spherical vesicles featuring positive turgor pressure. Corresponding *in vitro* experiments in our laboratories with human tumor cells (u87 glioblastoma) are underway and will be reported elsewhere.

## Acknowledgements

The authors gratefully acknowledge financial support from the Fraunhofer-Gesellschaft, Germany, through Vintage grant No. 600040 (Shock-Waves in Soft Biological Matter) and MAVO grant No. 400017 (Extracorporeal Focused Ultrasound Therapy). The authors thank Ulf Kahlert of the University Hospital Freiburg (Department of Neurosurgery) for fruitful discussions.

## References

- 1 T. Kodama, M. R. Hamblin and A. G. Doukas, *Biophys. J.*, 2000, **79**, 1821–1832.
- 2 A. G. Doukas, D. J. McAuliffe, S. Lee, V. Venugopalan and T. J. Flotte, *Ultrasound Med. Biol.*, 1995, **21**, 961–967.
- 3 A. G. Doukas and T. J. Flotte, *Ultrasound Med. Biol.*, 1996, **22**, 151–164.
- 4 S. E. Mulholland, S. Lee, D. J. McAuliffe and A. G. Doukas, *Pharm. Res.*, 1999, **16**, 514–518.
- 5 S. Lee and A. G. Doukas, *IEEE J. Sel. Top. Quantum Electron.*, 1999, **5**, 997–1003.
- 6 T. Kodama, A. G. Doukas and M. R. Hamblin, *Biochim. Biophys. Acta, Mol. Cell Res.*, 2002, **1542**, 186–194.
- 7 F. Brümmer, T. Bräuner and D. F. Hülser, *World J. Urol.*, 1990, **8**, 224–232.
- 8 C. C. Coussios and R. A. Roy, *Annu. Rev. Fluid Mech.*, 2008, **40**, 395–420.
- 9 M. P. Allen and D. J. Tildesley, *Computer simulation of liquids*, Clarendon Press, Oxford, 1987.
- 10 D. C. Rapaport, *The art of molecular dynamics simulation*, Cambridge University Press, 2004, p. 568.
- 11 S. J. Marrink, E. Lindahl, O. Edholm and A. E. Mark, *J. Am. Chem. Soc.*, 2001, **123**, 8638–8639.
- 12 K. Koshiyama, T. Kodama, T. Yano and S. Fujikawa, *Biophys. J.*, 2006, **91**, 2198–2205.
- 13 K. Koshiyama, T. Kodama, T. Yano and S. Fujikawa, *Biochim. Biophys. Acta, Biomembr.*, 2008, **1778**, 1423–1428.
- 14 M. O. Steinhauser, *Recent Res. Devel. Physics*, 2006, **7**, 56–97.
- 15 M. O. Steinhauser, *Computational multiscale modeling of fluids and solids: theory and applications*, Springer, Berlin, Heidelberg, New York, 2008.
- 16 S. J. Marrink, H. J. Risselada, S. Yefimov, D. P. Tieleman and A. H. de Vries, *J. Phys. Chem. B*, 2007, **111**, 7812–7824.
- 17 G. Stoltz, *Europhys. Lett.*, 2006, **76**, 849–855.
- 18 P. J. Hoogerbrugge and J. M. V. A. Koelman, *Europhys. Lett.*, 1992, **19**, 155–160.
- 19 P. Espanol and P. Warren, *Europhys. Lett.*, 1995, **30**, 191–196.
- 20 J. B. Avalos and A. D. Mackie, *Europhys. Lett.*, 1997, **40**, 141–146.
- 21 P. Espanol, *Europhys. Lett.*, 1997, **40**, 631–636.
- 22 I. Cooke, K. Kremer and M. Deserno, *Phys. Rev. E*, 2005, **72**, 011506.
- 23 S.-W. Chiu, H. L. Scott and E. Jakobsson, *J. Chem. Theory Comput.*, 2010, **6**, 851–863.
- 24 B. L. Holian and P. S. Lomdahl, *Science*, 1998, **280**, 2085–2088.
- 25 M. O. Steinhauser, K. Grass, E. Strassburger and A. Blumen, *Int. J. Plasticity*, 2009, **25**, 161–182.
- 26 I. Vattulainen, M. Karttunen, G. Besold and J. M. Polson, *J. Chem. Phys.*, 2002, **116**, 3967.
- 27 H. J. C. Berendsen, D. van der Spoel and R. van Drunen, *Comput. Phys. Commun.*, 1995, **91**, 43–56.
- 28 S. Plimpton, *J. Comput. Phys.*, 1995, **117**, 1–19.
- 29 U. Seifert, *Adv. Phys.*, 1997, **46**, 13–137.
- 30 K. Olbrich, W. Rawicz, D. Needham and E. Evans, *Biophys. J.*, 2000, **79**, 321–327.
- 31 C.-H. Lee, W.-C. Lin and J. Wang, *Phys. Rev. E*, 2001, **64**, 020901.
- 32 H. J. C. Berendsen, J. P. M. Postma, W. F. van Gasteren and J. Hermans, *Intermolecular Forces*, Reidel, Dordrecht, 1981.
- 33 V. Singh, A. Madan, H. Suneja and D. Chand, *Proc. Indian Acad. Sci.*, 1980, **3**, 169–175.
- 34 J. P. Hansen and I. R. McDonald, *Theory of simple liquids*, Academic Press, 2006.
- 35 E. Egberts and H. J. C. Berendsen, *J. Chem. Phys.*, 1988, **89**, 3718.